Journal of
Applied Physics

Combination of optical emission spectroscopy and multivariate data analysis techniques as a versatile non-invasive tool for characterizing xenon/krypton mixed gas plasma inside operating ion thrusters

Cite as: J. Appl. Phys. **131**, 053301 (2022); https://doi.org/10.1063/5.0074412
Submitted: 08 October 2021 • Accepted: 11 January 2022 • Published Online: 02 February 2022

Benny Nauschütt, Limei Chen, Kristof Holste, et al.

AIP Publishing

Journal of
Applied Physics ARTICLE scitation.org/journal/jap

Combination of optical emission spectroscopy and multivariate data analysis techniques as a versatile non-invasive tool for characterizing xenon/krypton mixed gas plasma inside operating ion thrusters

Cite as: J. Appl. Phys. **131**, 053301 (2022); doi: 10.1063/5.0074412
Submitted: 8 October 2021 · Accepted: 11 January 2022 ·
Published Online: 2 February 2022

Benny Nauschütt,[a)] Limei Chen, Kristof Holste, and Peter J. Klar

AFFILIATIONS

Institute of Experimental Physics I and Center of Materials Research (ZfM/Lama), Justus Liebig University, Heinrich-Buff-Ring 16, 35392 Giessen, Germany

Note: This paper is part of the Special Topic on Physics of Electric Propulsion.

[a)] **Author to whom correspondence should be addressed:** Benny.Nauschuett@physik.uni-giessen.de

ABSTRACT

Non-invasive assessment of the plasma parameters is a useful tool for a reliable characterization of many electric thrusters for space applications. Due to high costs, limited availability, and growing use of electric propulsion in spaceflight, alternatives to Xe as a propellant are becoming increasingly important. One option is to use the lighter noble gas krypton or xenon/krypton gas mixtures as a propellant. We propose a versatile analytical approach for establishing empirical correlations between plasma parameters and optical emission (OE) spectroscopy utilizing principal component analysis (PCA). Our approach allows us to establish a surjective mapping of individual OE spectra via their PCA scores onto the corresponding plasma parameters. We prove the feasibility of this approach for Xe, Kr, and Xe/Kr mixed plasmas demonstrating that it is applicable for a wide range of propellant candidates. A major advantage is that the approach does not rely on any microscopic modeling of the OE spectra of the plasma. After having established corresponding reference mappings, the approach can be explored for determining non-invasively and spatially resolved plasma parameters of the propellant plasma of various kinds of operating ion thrusters, which operate in the same plasma regime as the reference plasma. Thus, this method may contribute to shorter qualification and testing times of ion thrusters.

I. INTRODUCTION

Nowadays, electric propulsion (EP) systems are an established option as spacecraft engines.[1,2] While they deliver less thrust compared to their chemical counterpart, EP systems excel due to their high fuel efficiency and the vast number of usable propellants yielding a large variability for implementing them in space mission scenarios. There are many types of EP thrusters that generate a propellant plasma in the process of generating thrust. To optimize a thruster without disturbing the plasma, it is favorable to characterize the plasma non-invasively.[3,4] Currently, mainly, xenon is used as a propellant due to its high mass, chemical inertness, and fairly low ionization energy. However, xenon is also a rare resource and correspondingly expensive.[5,6] Thus, alternatives are sought, such as diluting or replacing xenon with the lighter and ten times more abundant noble gas krypton.[7–12] However, the properties of the plasma operated inside the thruster will change when altering the propellant used. Consequently, the operational points of the thruster need to be adjusted. This re-optimization may even require hardware adaptations.[7,11,12]

The radio-frequency ion thruster (RIT) is one of these established EP systems and was developed at the Justus Liebig University of Giessen in the 1960s.[13,14] The plasma discharge in a RIT is achieved by inductive heating of the electrons. When leaving the thruster, positive ions are accelerated by at least two extraction grids to generate a directed ion beam and, therefore, thrust according to Newton's third law.[1,2,15] The functioning of the ion optics of a RIT is determined by the interplay of plasma parameters of the propellant plasma inside the discharge vessel and the grid system. In other words, the geometry of the grid system alone does not define the ion optics. The shape of the plasma meniscus at the grid apertures of the screen grid depends on the plasma parameters and determines the divergence of the ion beamlet inside the grid system.[15] A wrong ion beam focusing leads to grid erosion by direct impingement and may drastically reduce the thruster's lifetime. Knowledge of the plasma parameters, in particular, electron temperature and density, at the actual operational points of the thruster is essential for a successful optimization of the thruster's performance.[15] During thruster qualification, non-invasive diagnostics, such as beam diagnostics, thrust measurement, performance data, and post- or mid-test erosion analysis, are commonly used to obtain information on the operating thruster.[16–18] In principle, invasive electrical probes can be used to determine plasma parameters[19,20] but are typically undesirable during qualification, as they may itself alter the plasma and, thus, affect the thruster's performance.[19] The plasma of gridded ion thrusters, in particular, will usually not be accessible with invasive probes, if no dedicated openings are available, since such extra openings are not desirable in a flight model; i.e., the grid system or the discharge vessel should not be altered.

Non-invasive alternatives for plasma characterization inside gridded ion thrusters need to be sought. A possible non-invasive diagnostics option is optical emission spectroscopy (OES), which can be used to assess plasma parameters of both beam and discharge by the application of a theoretical plasma model.[4,21–28] We recently introduced a method that utilizes non-invasive OES to assess plasma parameters of a thruster operating with xenon non-invasively by applying an empirical correlation between plasma parameters and OES instead of a theoretical model.[29] This method utilizes a principal component analysis (PCA)[30] and does not rely on any microscopic input other than the measurement of plasma parameters and OE spectra in a reference setup. Since it only requires optical access to the plasma, an OES-based method may be used during terrestrial testing for thruster development or space qualification in cases where an invasive probe cannot be employed. With the plasma parameters provided by this method, grid erosion can be estimated during testing already in the case of gridded ion thrusters. Depending on the type of thruster, an optical probe can be placed strategically to avoid interaction with the plume, allowing one to monitor the thruster with OES and beam diagnostics simultaneously. The high spatial resolution achievable in optical spectroscopy may allow establishing spatial maps of the plasma parameters of an inhomogeneous plasma. An example, where this may be of interest, is the mapping of the radial distribution of plasma parameters inside the discharge vessel of gridded ion thrusters, such as RITs.

In principle, plasma parameters can be extracted from OES using theoretical modeling of the electronic states of the atoms and ions responsible for the optical emission. Such theoretical plasma models can be found, e.g., for argon[31–44] and xenon,[4,21,22,24–27,41,45–47] but rarely for gas mixtures where even more microscopic processes need to be accounted for in order to obtain a reliable description. There are some studies in which theoretical models were applied to gas mixtures, but those focus on electron excitation only.[41,48–51] One exception is Ref. 52, which also considers several atom and molecule collision mechanisms. Such theoretical models are typically set up with a specific application in mind. The specifics of the application will be reflected by the number of electronic states and the selection of the microscopic processes between the species of the plasma, which are taken into account. Taking xenon as an example, Ref. 53 lists 443 electronic states just for neutral xenon, 161 for Xe^{+}, 157 for Xe^{2+}, and more for even higher ionization levels. The amount of electronic states used for theoretical models varies, e.g., 173 states in Ref. 24 or 38 states in Ref. 47. This means that the models are not easily transferable to other applications where the macroscopic excitation and discharge conditions of the plasma have changed. In particular, this also applies for gas mixtures. Adding another atomic species to a propellant, such as krypton to xenon, requires an accurate description of the electronic states of both species and corresponding ions similar to Refs. 41, 48, and 52. Furthermore, an entirely different set of microscopic processes between the xenon and krypton species comes into play, as for describing xenon–krypton collisions and excitation transfer.[54–58] A mixed gas model that includes such transfer mechanisms for argon and nitrogen is shown in Ref. 52. The missing parameters, such as cross sections, etc., are difficult to predict with *ab initio* theories and hard to determine experimentally.[59–64]

Here, we demonstrate that our non-invasive approach for determining plasma parameters is easily transferable to more sophisticated plasmas, such as those of gas mixtures of xenon and krypton. In future studies, this method might be applied to iodine plasmas as well, as iodine is another promising alternative to xenon as a propellant.[65,66] We demonstrate that the challenges met when attempting a microscopic description of such plasmas can be circumvented by our approach, and the plasma parameters can be reliably extracted.

II. EXPERIMENTAL DETAILS

The experimental setup used is shown in Fig. 1. The plasma is generated in a cylindrical RIT-10 (10 cm diameter) quartz glass

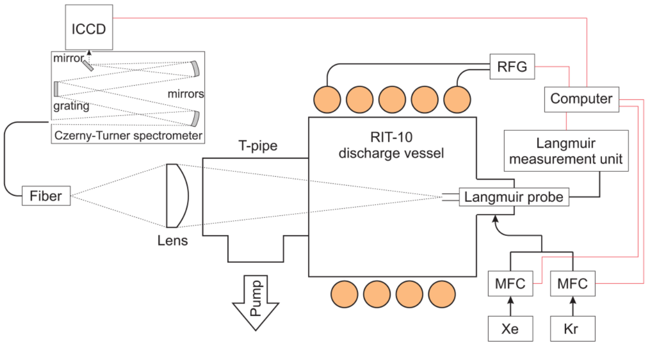

FIG. 1. Experimental setup for simultaneous measurement of the optical emission spectrum and the plasma parameters via a Langmuir double probe at the same position. The connections to the computer are shown as red lines. The setup is a modified version of the setup used in the previous work[29] yielding higher accuracy and allowing for the operation with mixed gases.

discharge vessel. The vessel has no extraction system and is operated without surrounding vacuum. Only the inside of the vessel is evacuated via the opening that holds the extraction system in a thruster arrangement. The magnetic field generated by the rf coil with six windings surrounding the vessel is not affected by the exposure to air as the relative permittivity of air and vacuum is almost identical.[67] The gas inlet is mounted on the opposite side of the vessel and also contains the Langmuir double probe to determine the electron temperature T_{e} and density n_{e}.[19,20,68,69]

The probe diagnostics were realized with a Keysight B2901A Precision Source/Measurement Unit as a four-wire measurement. The measurement range was −100 to 100 V (potential difference between the two probe wires) with voltage steps of 0.1 V and an integration time of 50 ms. The uncertainty for voltage and current measurement is given in the data sheet of the instrument with ±0.015% and ±0.02%, respectively. The Langmuir probe was built in-house and consists of two cylindrical wires of length 6.90 ± 0.1 mm and a radius of 0.125 ± 0.0125 mm. The spacing between the wires was 1.425 ± 0.025 mm.

The optical access to the discharge vessel is given by a glass window, and the focus of the detection optics is positioned in close vicinity of the Langmuir probe. The omission of the extraction system probably causes differences in the gas density distribution. Therefore, it is important to perform OES and Langmuir diagnostics on the same spot so that the correlation can be transferred to a real thruster with different gas density distributions with minimal error. The used 0.5 m Czerny–Turner spectrometer is connected to an intensified charge-coupled device (ICCD) camera (Princeton Instruments PI-MAX 4 1024f). The ICCD is capable of both continuous-wave (cw) and time-resolved measurements on the nanosecond scale but was only used for cw-measurements here. We chose a spectral window from 808 to 837 nm as it contains some of the fastest decaying spectral transitions for both neutral xenon and krypton.[70] Examples for xenon and krypton spectra are shown in Fig. 2. The observed optical transitions and feeding transitions of a potential transition chain are listed in Table I. All of the observed spectral transitions have relaxation times shorter than the period of the rf cycle, most of them by about an order of magnitude. The spectral resolution in the observed wavelength region is approximately 28 pm/pixel. The spectra were measured with 500 μs integration time and were averaged 10 000 times. The ICCD's intensifier was set to 1. We found a standard deviation of 1%–2% relative to the average counts for the background region and up to 5% at the peak positions. The response correction was performed with an AVALIGHT-HAL-CAL-MINI calibration source. The gas flow into the discharge vessel is controlled by a set of gas flow controllers (MFC), one for xenon (Bronkhorst EL-Flow F-200CV-AAA-11-V) and another for krypton (Bronkhorst EL-Flow select F-200CV-002-AAD-00-V). Both MFCs have a maximum flow range of 1.5 sccm xenon. The MFC calibration with the used gases (Kr 5.0 and Xe 4.0) was performed with a Mettler Toledo ME503T/00 scale with a mounted gas reservoir. In this calibration process, the reservoir is evacuated and then filled by setting a constant mass flow on the MFC under calibration. The measured weight is recorded until a total mass of 150 mg is accumulated. This measurement was done for four different gas flows for both MFCs. A linear fit of the weight over time measurements yields the actual gas flow. A linear fit of the actual gas flows over the nominal gas flows yields the calibration function. The accuracy of the calibration was about 0.1 % for xenon and about 1.5 % for krypton. The plasma was excited by a half-bridge radio-frequency generator (RFG)[71,72] at a resonance frequency around 1.6 MHz corresponding to a period of the rf cycle of 625 ns. The RFG input power was delivered by an Aim TTi CPX400DP power source, and the frequency was measured with a GW Instek GDS-2204E oscilloscope. The RFG input power was varied while keeping the gas flow constant. The experiments were performed for various combinations of xenon and krypton gas flows. The plasma was operated for 5 min at each operational point before starting the measurement to ensure thermal stability during roughly 2 min of measurement time. After changing the gas flow settings, the plasma was allowed to settle for 12 min before commencing the measurements.

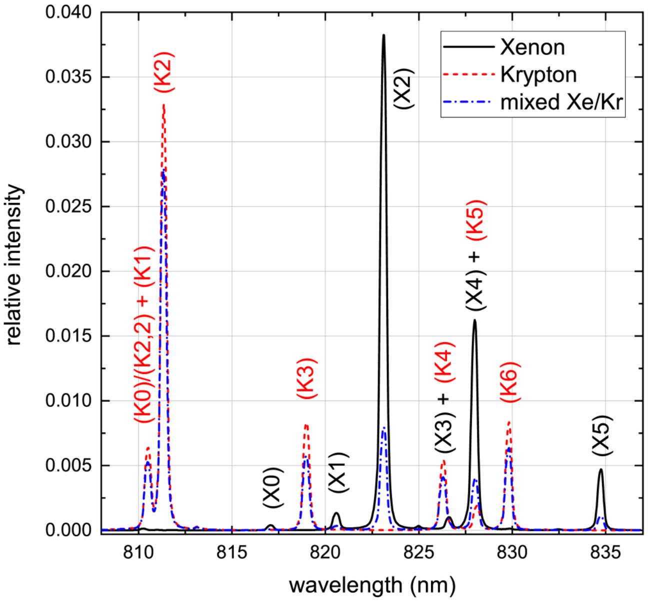

FIG. 2. Example spectra for both xenon and krypton as well as mixed gas plasma. Additional information about the individual lines can be found in Table I. The shown spectra are intensity-normalized.

In a previously conducted measurement series, we used the glass vessel with an easy optical access to the plasma from behind.[29] The setup was rearranged and improved in order to allow detection of the plasma emission from a spot close to the Langmuir probe. The rearrangement of the setup further increases the reliability of the measurement approach. The previously used spectral window from 820 to 840 nm[29] was shifted slightly toward shorter wavelengths (808–837 nm), thus sacrificing one small xenon line in favor of a strong krypton double line (K0+K1 and K2 in Fig. 2).

A. Principal component analysis

To analyze the behavior of the relative line intensities for different operational points of the plasma of a species or gas mixture, we

TABLE I. Wavelengths, relaxation times, intensities, and the involved electronic states of the observed transitions shown in Fig. 2 are listed for both xenon[53,70] and krypton.[70,73] The listed intensities are only the qualitative values from Refs. 53 and 73. Using the index, the transitions can be found in Fig. 2. The observed transitions are also shown in bold.

				Lower level			Upper level		
Index	Wavelength (nm)	Relaxation time (ns)	Intensity	Configuration	Term	J	Configuration	Term	J
(X0)	**817.10**	**n.a.**	**100**	**$5p^5(^2P^\circ_{3/2})6p$**	**$^2[3/2]$**	**2**	**$5p^5(^2P^\circ_{1/2})5d$**	**$^2[3/2]^\circ$**	**2**
(X0,1)	722.26	n.a.	20	$5p^5(^2P^\circ_{1/2})5d$	$^2[3/2]^\circ$	2	$5p^5(^2P^\circ_{1/2})6f$	$^2[5/2]$	3
(X0,2)	800.96	n.a.	30	$5p^5(^2P^\circ_{1/2})5d$	$^2[3/2]^\circ$	2	$5p^5(^2P^\circ_{1/2})5f$	$^2[5/2]$	3
(X1)	**820.63**	**50**	**700**	**$5p^5(^2P^\circ_{1/2})6s$**	$^2[1/2]^\circ$	**0**	**$5p^5(^2P^\circ_{1/2})6p$**	**$^2[3/2]$**	**1**
(X1,1)	3605.49	1700	20	$5p^5(^2P^\circ_{1/2})6p$	$^2[3/2]$	1	$5p^5(^2P^\circ_{1/2})5d$	$^2[5/2]^\circ$	2
(X2)	**823.16**	**35**	**10000**	**$5p^5(^2P^\circ_{3/2})6s$**	**$^2[3/2]^\circ$**	**2**	**$5p^5(^2P^\circ_{3/2})6p$**	$^2[3/2]$	**2**
(X2,1)	3107.77	1400	6000	$5p^5(^2P^\circ_{3/2})6p$	$^2[3/2]$	2	$5p^5(^2P^\circ_{3/2})5d$	$^2[5/2]^\circ$	3
(X2,2)	1672.82	556	5000	$5p^5(^2P^\circ_{3/2})6p$	$^2[3/2]$	2	$5p^5(^2P^\circ_{3/2})7s$	$^2[3/2]^\circ$	2
(X2,3)	739.38	204	150	$5p^5(^2P^\circ_{3/2})6p$	$^2[3/2]$	2	$5p^5(^2P^\circ_{3/2})7d$	$^2[5/2]^\circ$	3
(X3)	**826.65**	**61.7**	**500**	**$5p^5(^2P^\circ_{1/2})6s$**	$^2[1/2]^\circ$	**1**	**$5p^5(^2P^\circ_{1/2})6p$**	**$^2[1/2]$**	**1**
(X3,1)	4610.87	3700	1	$5p^5(^2P^\circ_{1/2})6p$	$^2[1/2]$	1	$5p^5(^2P^\circ_{1/2})5d$	$^2[3/2]^\circ$	2
(X4)	**828.01**	**27.1**	**7000**	**$5p^5(^2P^\circ_{3/2})6s$**	**$^2[3/2]^\circ$**	**1**	**$5p^5(^2P^\circ_{3/2})6p$**	**$^2[1/2]$**	**0**
(X4,1)	1878.82	1100	860	$5p^5(^2P^\circ_{3/2})6p$	$^2[1/2]$	0	$5p^5(^2P^\circ_{3/2})7s$	$^2[3/2]^\circ$	1
(X4,2)	2651.77	6300	30	$5p^5(^2P^\circ_{3/2})6p$	$^2[1/2]$	0	$5p^5(^2P^\circ_{3/2})5d$	$^2[3/2]^\circ$	1
(X5)	**834.68**	**24**	**2000**	**$5p^5(^2P^\circ_{1/2})6s$**	**$^2[1/2]^\circ$**	**1**	**$5p^5(^2P^\circ_{1/2})6p$**	**$^2[3/2]$**	**2**
(X5,1)	3869.68	1900	200	$5p^5(^2P^\circ_{1/2})6p$	$^2[3/2]$	2	$5p^5(^2P^\circ_{1/2})5d$	$^2[5/2]^\circ$	3
(K0)	**810.40**	**153**	**500**	$4s^24p^5(^2P^\circ_{3/2})5p$	$^2[5/2]$	**3**	$4s^24p^5(^2P^\circ_{3/2})5d$	$^2[7/2]^\circ$	**4**
(K1)	**810.44**	**112**	**4000**	**$4s^24p^5(^2P^\circ_{3/2})5s$**	$^2[3/2]^\circ$	**2**	**$4s^24p^5(^2P^\circ_{3/2})5p$**	**$^2[5/2]$**	**2**
(K1,1)	1317.74	204	310	$4s^24p^5(^2P^\circ_{3/2})5p$	$^2[5/2]$	2	$4s^24p^5(^2P^\circ_{3/2})6s$	$^2[3/2]^\circ$	1
(K1,2)	1362.24	201	130	$4s^24p^5(^2P^\circ_{3/2})5p$	$^2[5/2]$	2	$4s^24p^5(^2P^\circ_{3/2})4d$	$^2[3/2]^\circ$	1
(K1,3)	1689.05	130	340	$4s^24p^5(^2P^\circ_{3/2})5p$	$^2[5/2]$	2	$4s^24p^5(^2P^\circ_{3/2})4d$	$^2[7/2]^\circ$	3
(K2)	**811.29**	**27.70**	**500**	**$4s^24p^5(^2P^\circ_{3/2})5s$**	$^2[3/2]^\circ$	**2**	**$4s^24p^5(^2P^\circ_{3/2})5p$**	**$^2[5/2]$**	**3**
(K2,1)	645.63	150	200	$4s^24p^5(^2P^\circ_{3/2})5p$	$^2[5/2]$	3	$4s^24p^5(^2P^\circ_{3/2})6d$	$^2[7/2]^\circ$	4
(K2,2)	810.40	153	500	$4s^24p^5(^2P^\circ_{3/2})5p$	$^2[5/2]$	3	$4s^24p^5(^2P^\circ_{3/2})5d$	$^2[7/2]^\circ$	4
(K2,3)	1363.42	97.1	250	$4s^24p^5(^2P^\circ_{3/2})5p$	$^2[5/2]$	3	$4s^24p^5(^2P^\circ_{3/2})6s$	$^2[3/2]^\circ$	2
(K3)	**819.01**	**112**	**300**	**$4s^24p^5(^2P^\circ_{3/2})5s$**	$^2[3/2]^\circ$	**1**	**$4s^24p^5(^2P^\circ_{3/2})5p$**	**$^2[3/2]$**	**2**
(K3,1)	985.62	251	500	$4s^24p^5(^2P^\circ_{3/2})5p$	$^2[3/2]$	2	$4s^24p^5(^2P^\circ_{1/2})4d$	$^2[3/2]^\circ$	2
(K3,2)	1537.20	680	725	$4s^24p^5(^2P^\circ_{3/2})5p$	$^2[3/2]$	2	$4s^24p^5(^2P^\circ_{3/2})6s$	$^2[3/2]^\circ$	2
(K3,3)	1678.51	148	320	$4s^24p^5(^2P^\circ_{3/2})5p$	$^2[3/2]$	2	$4s^24p^5(^2P^\circ_{3/2})4d$	$^2[5/2]^\circ$	3
(K4)	**826.32**	**29.27**	**400**	**$4s^24p^5(^2P^\circ_{1/2})5s$**	$^2[1/2]^\circ$	**1**	**$4s^24p^5(^2P^\circ_{1/2})5p$**	**$^2[3/2]$**	**2**
(K4,1)	1006.60	3770	10	$4s^24p^5(^2P^\circ_{1/2})5p$	$^2[3/2]$	2	$4s^24p^5(^2P^\circ_{3/2})6d$	$^2[7/2]^\circ$	3
(K4,2)	1388.29	94.3	27	$4s^24p^5(^2P^\circ_{1/2})5p$	$^2[3/2]$	2	$4s^24p^5(^2P^\circ_{1/2})6s$	$^2[1/2]^\circ$	1
(K5)	**828.11**	**70.52**	**200**	**$4s^24p^5(^2P^\circ_{1/2})5s$**	**$^2[1/2]^\circ$**	**1**	**$4s^24p^5(^2P^\circ_{1/2})5p$**	**$^2[1/2]$**	**1**
(K5,1)	1012.10	1600	30	$4s^24p^5(^2P^\circ_{1/2})5p$	$^2[1/2]$	1	$4s^24p^5(^2P^\circ_{3/2})6d$	$^2[3/2]^\circ$	2
(K5,2)	1383.29	321	8	$4s^24p^5(^2P^\circ_{1/2})5p$	$^2[1/2]$	1	$4s^24p^5(^2P^\circ_{1/2})6s$	$^2[1/2]^\circ$	1
(K5,3)	1393.90	90.9	10	$4s^24p^5(^2P^\circ_{1/2})5p$	$^2[1/2]$	1	$4s^24p^5(^2P^\circ_{1/2})6s$	$^2[1/2]^\circ$	0
(K6)	**829.81**	**34.12**	**500**	**$4s^24p^5(^2P^\circ_{3/2})5s$**	**$^2[3/2]^\circ$**	**1**	**$4s^24p^5(^2P^\circ_{3/2})5p$**	**$^2[3/2]$**	**1**
(K6,1)	1442.68	108	350	$4s^24p^5(^2P^\circ_{3/2})5p$	$^2[3/2]$	1	$4s^24p^5(^2P^\circ_{3/2})6s$	$^2[3/2]^\circ$	1
(K6,2)	1496.19	1110	290	$4s^24p^5(^2P^\circ_{3/2})5p$	$^2[3/2]$	1	$4s^24p^5(^2P^\circ_{3/2})4d$	$^2[3/2]^\circ$	1
(K6,3)	1693.58	173	280	$4s^24p^5(^2P^\circ_{3/2})5p$	$^2[3/2]$	1	$4s^24p^5(^2P^\circ_{3/2})4d$	$^2[5/2]^\circ$	2

performed a PCA[30] of all recorded spectra at up to several hundreds of operational points. The PCA technique reduces the dimensions of a dataset with a large number of measured variables. This simplifies the process of correlating the spectral information and the corresponding plasma parameters significantly. PCA is not the only technique capable of dimension reduction. Other methods include linear discriminant analysis,[74] non-negative matrix factorization,[75] and factor analysis.[76] However, we only focus on the PCA here.

For establishing an empirical correlation between OES and plasma parameters, a reference dataset is measured, consisting of a total of m spectra. Each spectrum consists of n data points or n wavelength positions and their respective spectral intensities. In other words, a spectrum is a point in an n-dimensional coordinate space, in which the n wavelength positions define the coordinate axes and the respective intensities are the coordinates on these axes. By performing a PCA, the n-dimensional coordinate space that contains the spectra is, for example, reduced into a two-dimensional coordinate space, in which the individual data points still are well separated. This two-dimensional coordinate space is spanned by two new axes, which typically contain the highest and second highest variance of the dataset.

The process of determining the PCA axes is described in the following. The covariances σ_{ij} of each of the n wavelength positions with every other wavelength position (including itself) are calculated using

$$\sigma_{ij} = \frac{1}{m} \times \sum_{k=0}^{m} (x_{ki} - \overline{x_i}) \times (x_{kj} - \overline{x_j}), \tag{1}$$

where x_{ki} and x_{kj} are the intensities of spectrum k at the two wavelength positions i and j. The variables $\overline{x_i}$ and $\overline{x_j}$ are the average intensities at the wavelength positions i and j of the average spectrum of all spectra of the recorded set.

With the covariances calculated, the covariance matrix $\mathbf{C}$ is set up as

$$\mathbf{C} = \begin{pmatrix} \sigma_{00} & \sigma_{01} & \cdots & \sigma_{0n} \\ \sigma_{10} & \sigma_{11} & \cdots & \sigma_{1n} \\ \vdots & \vdots & \ddots & \vdots \\ \sigma_{n0} & \sigma_{n1} & \cdots & \sigma_{nn} \end{pmatrix}. \tag{2}$$

The eigenvalues of $\mathbf{C}$ correspond to the data variances on the principal component axes $PC_{\mathrm{E},i}(\lambda)$, which are the eigenvectors of $\mathbf{C}$ and are spectrum-like with n components.

The coordinates (or scores) of a spectrum $S(\lambda)$ in this new coordinate system of $PC_{\mathrm{E},i}(\lambda)$ are calculated as follows:

$$PC_i = \sum_{\lambda} (S(\lambda) - \overline{S_{\mathrm{PCA}}}(\lambda)) \times PC_{\mathrm{E},i}(\lambda), \tag{3}$$

where $\overline{S_{\mathrm{PCA}}}$ is the average spectrum of the reference dataset. The spectrum $S(\lambda)$ can now be written as a series expansion,

$$S(\lambda) = \overline{S_{\mathrm{PCA}}}(\lambda) + \sum_{i} PC_i \times PC_{\mathrm{E},i}(\lambda). \tag{4}$$

The fraction in percent of the total variance on each axis shows how much of the variation in the data is represented by the scores of this principal component. Often, the sum the variances on PC_1 and PC_2 is already close to 100% of the total variance so that the data can be sufficiently separated in just two dimensions.

B. Evaluation of the Langmuir probe measurements

The Langmuir probe measurements were evaluated using a modified version of the standard procedure.[19,20,68,69] This modified approach is more robust against deviations from the theoretical ideal. It was developed in the course of our previously reported experiments[29] on the basis of the standard procedure.[19,20,68,69] The process is shown in Fig. 3, where the first step is the determination of the ion saturation current I_{sat}. I_{sat} is the intercept of a linear fit $[f(U) = a \times U + I_{\mathrm{sat}}]$ in the saturation regions shown as red dashed lines in Fig. 3. To correct for the saturation, the slope a is subtracted from the U–I-characteristics $[I_{\mathrm{corrected}}(U) = I(U) - a \times U]$, and the dashed blue curve in Fig. 3 is obtained. The corrected curve $I_{\mathrm{corrected}}(U)$ is normalized by dividing by I_{sat} (not shown in Fig. 3 for simplicity). The maximum slope s_{max} of the normalized, corrected curve is proportional to the inverse electron temperature T_{e}. s_{max} is obtained by a polynomial fit of third order $[f(x) = \sum_{i=0}^{3} a_i \times x^i]$ in the region $-\Delta U$ to $+\Delta U$; therefore, $s_{\mathrm{max}} = -\frac{1}{3} a_2^2 / a_3 + a_1$. The electron temperature in Kelvin is calculated according to

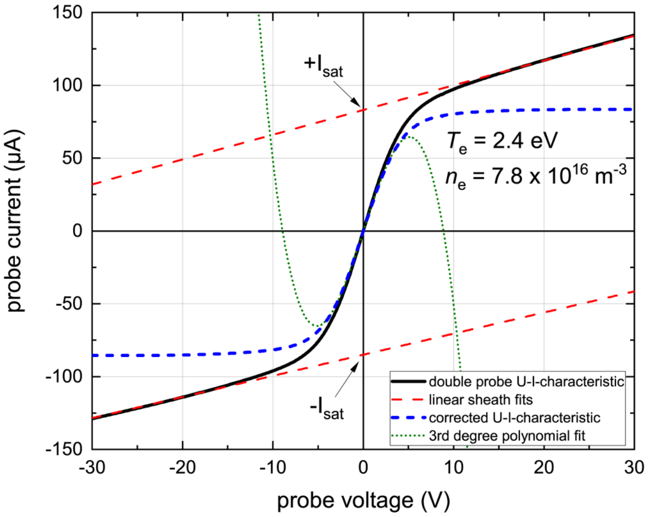

FIG. 3. Langmuir double probe evaluation process illustrated for measurement data of a pure xenon plasma. The linear parts of the measured curve (black line) are fitted to obtain the ion saturation current I_{sat} (red dashed lines). The probe voltage U is the potential difference between the two probe wires. The curve is corrected (dashed blue line), and the maximum slope is determined by fitting a third order polynomial (dotted green line) in the vicinity of $U = 0$ V. The plasma parameters T_{e} and n_{e} are calculated using Eqs. (5) and (6).

$$T_{\mathrm{e}} = \frac{e}{2 k_{\mathrm{B}} \times s_{\mathrm{max}}}. \tag{5}$$

To calculate the electron density n_{e}, the previously determined values I_{sat} and T_{e}, as well as the probe area A_{p}, and the ion mass m_{ion} are needed,

$$n_{\mathrm{e}} = \frac{I_{\mathrm{sat}}}{A_{\mathrm{p}} e} \sqrt{\frac{m_{\mathrm{ion}}}{k_{\mathrm{B}} T_{\mathrm{e}}}}. \tag{6}$$

An additional approximation is necessary when the electron density n_{e} has to be calculated for mixed gas plasmas using Eq. (6). The ion mass m_{ion} is not easily determined, as the mixture consists of the two main ion species Xe$^+$ and Kr$^+$, which both contribute to the measured Langmuir U–I-characteristics. We, therefore, use an approximated effective ion mass $m_{\mathrm{ion,eff}}$ for the calculation of n_{e}. Since the gas flow Q in sccm represents the number of particles inserted into the discharge chamber, we can calculate the weighted average atomic mass $m_{\mathrm{atom,eff}}$ as

$$m_{\mathrm{atom,eff}} = m_{\mathrm{Xe}} \times \frac{Q_{\mathrm{Xe}}}{Q_{\mathrm{Xe}} + Q_{\mathrm{Kr}}} + m_{\mathrm{Kr}} \times \frac{Q_{\mathrm{Kr}}}{Q_{\mathrm{Xe}} + Q_{\mathrm{Kr}}}, \tag{7}$$

assuming equal residence times of the two atomic species inside the discharge chamber. While the exact gas flow does not matter for the evaluation of Langmuir measurements on a pure gas plasma, mixed gas plasmas require calibrated MFCs to avoid errors when employing Eq. (7). If we further assume the ionization degree for xenon and krypton to be identical, effective atomic mass and effective ion mass will be equal ($m_{\mathrm{atom,eff}} = m_{\mathrm{ion,eff}}$). However, in reality, krypton will have a shorter residence time due to its smaller mass and, therefore, a higher thermal velocity. Furthermore, the higher ionization energy of krypton will result in a lower ionization degree than for xenon. Both effects will push the real effective ion mass further toward that of xenon. Therefore, the real n_e will be probably somewhat higher than estimated. However, our assumptions should be sufficient to demonstrate the basic principle of our approach without going deeper into ionization processes and particle motion.

The definition of a temperature assumes a Maxwellian electron energy distribution function (EEDF).[19,20,68] In an rf plasma, the fast electrons in the Maxwell tail are suppressed; therefore, the EEDF can deviate from the Maxwellian ideal.[37,77] This also changes the optical spectrum, as excitation rates change. Our empirical approach builds a correlation on a set of experimental data of a real plasma. Thus, as long as another real plasma analyzed on the basis of our reference data is comparable to the one used for acquiring the reference data (which shall be the case, if the optical emission spectra are comparable), the specific EEDF is not too relevant for the outcome of the analysis. We assume that a spectrum will be comparable to the reference spectra, if the plasma under study is driven under comparable experimental conditions (i.e., rf frequency and power, neutral gas densities of the propellant mixture) and if all relative line intensities are within the range of the mapped line intensities. If the PCA scores then fall inside the reference PCA, the correlation will be applicable. However, it should be noted that the validity of the application to a plasma in a setup other than the reference setup is not investigated here. It is yet unclear whether differences in the setup may affect the applicability.

III. RESULTS AND DISCUSSION

During the acquisition of a series of hundreds of spectra, small vibrations or thermal expansion of the measurement equipment might cause small wavelength shifts of the optical transitions of some tens of picometers. Here, the spectra shifted by approximately 1 pixel or 28 pm over the full measurement series. While they are not relevant for the evaluation, the PCA may be sensitive to such shifts. To circumvent the issue, the spectral information is simplified by integrating the line intensities of the, e.g., six xenon lines shown in Fig. 2. For example, the line intensity of X2 at 823.16 nm is determined by adding up all measured intensities between 821.99 and 824.11 nm. The PCA is then performed with these line intensities as input. The obtained principal components $PC_{\mathrm{E},i}$ ($i = 1, \ldots, 6$ for xenon) are the new coordinate axes with maximum data spread, where $PC_{\mathrm{E},1}$ covers the highest variance, followed by $PC_{\mathrm{E},2}$, etc.

First, we conducted measurements on a pure xenon plasma at various gas flows and input powers. $PC_{\mathrm{E},1}$ and $PC_{\mathrm{E},2}$ cover the majority of the data variance. However, due to a wide range of rf power, the first two principal components are not fully sufficient to separate the spectra in the corresponding 2D representation for all operational points of the plasma, with each spectrum corresponding to another set of plasma parameters. To fully separate the spectra, the third axis $PC_{\mathrm{E},3}$ also has to be considered. For this purpose, we define a new axis direction in the PC_1/PC_2 plane as a linear combination of PC_1 and PC_2 defined by the vector $\vec{v}$,

$$x_v = \begin{pmatrix} v_1 \\ v_2 \end{pmatrix} \cdot \begin{pmatrix} PC_1 \\ PC_2 \end{pmatrix} = v_1 \times PC_1 + v_2 \times PC_2. \tag{8}$$

Choosing $v_1 = -1/3$ and $v_2 = 1$ in this case yields a satisfactory separation of the data points (each corresponding to a spectrum of a specific operational point of the plasma) when plotting the corresponding scores in a projected 2D representation PC_3 vs $(-1/3PC_1 + PC_2)$ as shown in Fig. 4(a). The scores in Fig. 4(a) reveal a regular pattern with clear trends as functions of the external input parameters, i.e., the rf power coupled into the plasma and the propellant gas flow defining the neutral gas density of the plasma. A variation of the gas density for a given power yields almost straight lines in the 2D plane, whereas the variation of the rf power at a fixed density leads to curves as indicated in the figure.

The corresponding plasma parameters shown in Fig. 4(b) measured simultaneously with the spectra exhibit the anticipated trends.[15,78,79] Lowering the xenon gas flow increases the electron temperature. The electron density increases with higher input power. The maximum electron density reached for lower gas flow decreases, as the input power limitation is reached earlier. An interesting pattern occurs at low input powers, where the mapping was done in small power steps. Here, the electron temperature rises with increasing electron density and falls off again exhibiting a sharp maximum at around $5 \times 10^{16}\,\mathrm{m}^{-3}$. Currently, we seek a satisfactory explanation for this behavior.

Having established a 2D representation in a 2D plane of the coordinate space in Fig. 4(a), which virtually separates the data points representing all spectra taken at different operational conditions and having shown in Fig. 4(b) that the plasma parameters T_e and n_e show the anticipated trends, we can now parameterize the dependence of T_e and n_e on the coordinates given by the chosen new axes. To describe the plasma parameters in Fig. 4(b) as a function of the scores shown in Fig. 4(a), we introduce the fitting function,

$$f(x_v, PC_3) = \sum_{i=0}^{n} \sum_{j=0}^{i+j\leq n} a_{i,j} \times x_v^i \times PC_3^j. \tag{9}$$

Here, x_v is the modified score value according to Eq. (8) and n is the polynomial order of the fit. Using the fitting function in Eq. (9) with a polynomial order of $n = 4$, the R^2-values for the T_e and n_e fits are 0.954 and 0.990, respectively. Since the function in Eq. (9)

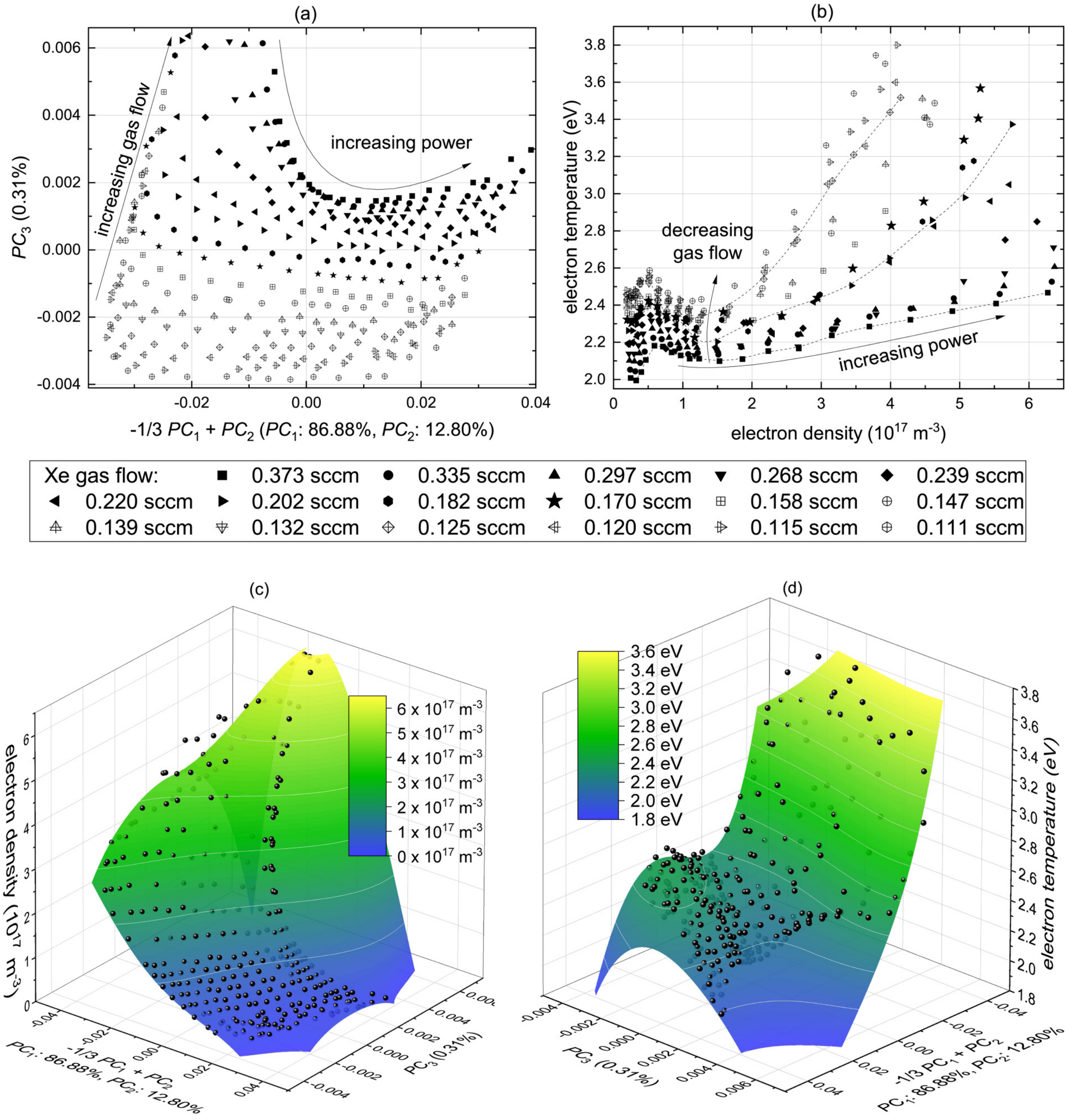

FIG. 4. PCA scores of a series of xenon spectra taken at various gas flows (a). The three-dimensional scores are displayed in two dimensions with the *x* axis being a vector on the PC_1–PC_2 plane to better visualize the spread in the OES data. The corresponding plasma parameters measured with the Langmuir double probe of the same series are shown in (b). The fits of the electron density (c) and the temperature (d) over the modified PCA scores are the correlation between OES and plasma parameters for pure xenon.

is three-dimensional, the fits can be displayed and are shown in Figs. 4(c) and 4(d). The two 3D plots clearly demonstrate that the PCA can indeed establish correlations between plasma parameters and the optical emission spectra. Of course, such a parameterization is best in the center of the set of data points and deviates toward the edges of the fitted 2D surface. In this measured dataset, we find the deviation between measured and calculated plasma parameters to be about ±5% for T_e and ±20% for n_e

when the edges of the contour fitting are avoided. For the anticipated application, i.e., the non-invasive determination of the plasma parameters inside an ion thruster, it will be of major importance that the operational points of its plasma lie well inside the parameter space of operational points of the reference plasma. However, if this is given, the plasma parameters can be determined non-invasively with a high degree of accuracy.

Using the same approach, we can also analyze the OES data for krypton plasmas. The data points corresponding to the optical emission spectra recorded at different operational points of the plasma can be separated quite well when plotting their PC scores in the plane spanned by PC_2 and PC_3 as shown in Fig. 5(a). However, there is no angle at which the first three principal component scores can be projected to a 2D representation without major overlapping of data points.

Nevertheless, the plot of the electron density n_e vs electron temperature T_e in Fig. 5(b) shows again clear trends as a function of rf power and gas flow. The electron temperatures reach higher levels than for xenon, while the electron densities are somewhat smaller. Due to the higher ionization energy of krypton, more energy is needed for heating of the electrons before ionization is possible. Therefore, a hotter, less dense plasma is expected.

Contrary to the xenon case, the two plasma parameters cannot be fitted to a fitting curve according to Eq. (9), as the overlapping shown in Fig. 5(a) prevents a direct surjective correspondence. One possibility to set up a parametric correlation is employing a higher dimensional fit, thus yielding $T_e(PC_1, PC_2, PC_3)$ and $n_e(PC_1, PC_2, PC_3)$. However, such a fit cannot be presented in a 3D plot. Therefore, we use an alternative approach. As the data cloud forms a 3D surface, another option is to find a parametric description of that surface with two variables u and v and to establish correlations $T_e(u, v)$ and $n_e(u, v)$. For this purpose, we created a mesh from the PCA results as shown in Fig. 5(a). We then assigned u and v values to the individual measurements according to their position on that mesh so that u increases with decreasing input power, while v increases with decreasing mass flow. The PCA scores can then be fitted as a function of the u–v coordinates as shown in Fig. 5(c). The corresponding plasma parameters shown in Fig. 5(b) can also be fitted as functions of the u–v coordinates as shown in Figs. 5(d) and 5(e). All fits were performed using fitting functions of the type,

$$f(u, v) = \sum_{i=0}^{n} \sum_{j=0}^{i+j\leq n} a_{i,j} \times u^i \times v^j, \tag{10}$$

with $n = 3$. The R^2 values were 0.978 for $PC_1(u, v)$, 0.986 for $PC_2(u, v)$, 0.991 for $PC_3(u, v)$, 0.918 for $T_e(u, v)$, and 0.997 for $n_e(u, v)$.

A new spectrum measured at an operational point where the plasma parameters shall be determined can now be transferred in the PCA coordinate space using Eq. (3). To obtain the plasma parameters for this operational point, the u–v coordinates have to be determined. By looking at the position of the corresponding PCA-point on the mesh shown in Fig. 5(a), u–v coordinates can be estimated. The u–v values can now be refined using the previously found functions $PC_i(u, v)$ and minimizing the sum of the relative quadratic deviations of the measured scores PC_i of the spectrum and the calculated scores $PC_i(u, v)$ using

$$\sum_{i=1}^{3} \left(\frac{PC_i - PC_i(u, v)}{PC_i} \right)^2 \rightarrow \text{min}. \tag{11}$$

The refined u–v values can then be used to obtain T_e and n_e using the previously found functions $T_e(u, v)$ and $n_e(u, v)$. This method is, however, somewhat reliant on the quality of the parameterization $PC_i(u, v)$ and a good first estimation of u and v. Especially toward the edges of the fitting regions, this method becomes less reliable. In our measured dataset, if good first estimations are used and the edges are avoided, we find the deviation between measured and calculated plasma parameters to be about $\pm 10\%$ for T_e and $\pm 25\%$ for n_e.

After having demonstrated that our approach is suitable for plasmas of pure xenon and krypton propellants, we will now turn to its use for analyzing plasmas of gas mixtures of xenon and krypton. The spectra of the xenon/krypton plasma shown in Fig. 2 indicate one of the challenges typical in analyzing OES data of mixed plasma. In the spectral window selected by us, the spectral lines of xenon and krypton, X3 and K4, and X4 and K5 overlap. We have handled this situation by considering these lines as one line in the simplification procedure prior to the PCA. Furthermore, we have performed multiple series of combined OES and Langmuir measurements where we have kept the krypton gas flow constant and varied the xenon gas flow. In other words, the mixing ratio is not constant throughout a series. We have acquired datasets for the four constant krypton gas flows 0.354, 0.218, 0.147, and 0.108 sccm. In what follows, we will exemplarily discuss the data set where the krypton gas flow was set to 0.218 sccm and the xenon gas flow was varied between about 0.1 and 0.4 sccm.

As for the pure propellants, the PCA results of the mixture allow one to separate all the data points corresponding to optical emission spectra taken at different operational conditions as shown in Fig. 6(a). Thus, the projection method could be employed similar to the pure xenon case. The projection plane was spanned by PC_2 and the linear combination of $-0.05PC_1 + PC_3$. Again, clear trends in the 2D plot can be observed as a function of increasing xenon flow as well as in dependence on rf power as indicated in Fig. 6(a).

The same holds for the plot of electron temperature T_e vs electron density n_e in Fig. 6(b). Characteristic curves are obtained as a function of added xenon gas flow and as a function of rf power. These resemble those obtained for the pure propellants.

As expected, the electron temperature rises with decreasing gas flow. However, the differences in the electron temperature for different xenon gas flows shown in Fig. 6(b) become smaller with decreasing xenon gas flows. The rise in the electron temperature is a result of lower neutral gas density, where the electrons acquire more energy per rf half cycle, as they have a lower probability to collide with atoms and ions. In this case, only the xenon gas flow of the gas mixture is lowered; therefore, only the neutral xenon density is reduced. Since the krypton gas flow remains constant, the overall neutral gas density approaches a constant value greater than zero. Decreasing the xenon gas flow from, e.g., 0.120 to 0.111 sccm, has less effect on the plasma parameters than in pure

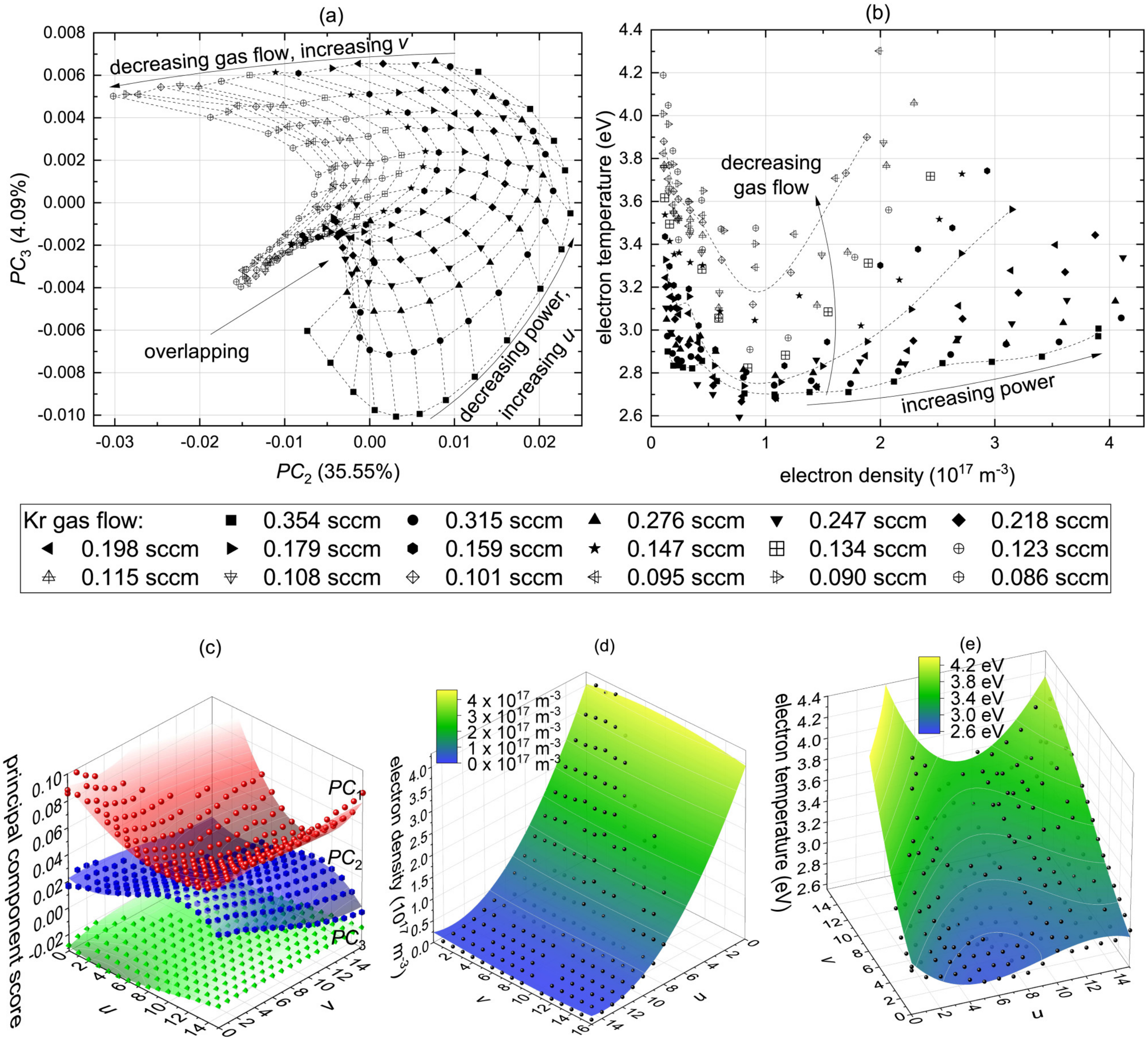

FIG. 5. PCA scores for a series of krypton spectra taken at various gas flows (a). The data spread can be seen best when observing the three-dimensional scores in the PC_2–PC_3 plane. The corresponding plasma parameters measured with the Langmuir double probe for this series are shown in (b). A fit for each principal component as a function of new coordinates u and v is shown in (c). The data points of PC_1 and PC_2 in (c) are shifted upward for a better visual representation. The values for the new variables u and v are assigned to the data points in the PCA coordinate space according to their position on the mesh shown in (a). The plasma parameters can also be fitted as functions of the u–v coordinates, as shown for electron density (d) and temperature (e). This yields a correlation between optical emission spectra and plasma parameters with one additional step to perform compared to the projection method used for xenon in Fig. 4.

xenon as the krypton atoms present as a background serve as collision partners for the electrons. Vice versa, a small portion of xenon in the plasma still provides enough easily ionizable atoms to keep the electron temperature below the ones shown in Fig. 5(b) for pure krypton.

These findings allow us to plot surfaces of the plasma parameters in dependence of the PCA based coordinates selected for achieving the separation into two dimensions in Fig. 6(a). The two surface fits of electron density n_e and electron temperature T_e are shown in Figs. 6(c) and 6(d), respectively. Here, Eq. (9) was applied with a polynomial order of $n = 4$, yielding an R^2 of 0.980 for n_e and 0.978 for T_e. In this mixed gas dataset, we find the deviation between measured and calculated plasma parameters to be about $\pm 5\%$ for T_e and $\pm 25\%$ for n_e when the edges of the contour

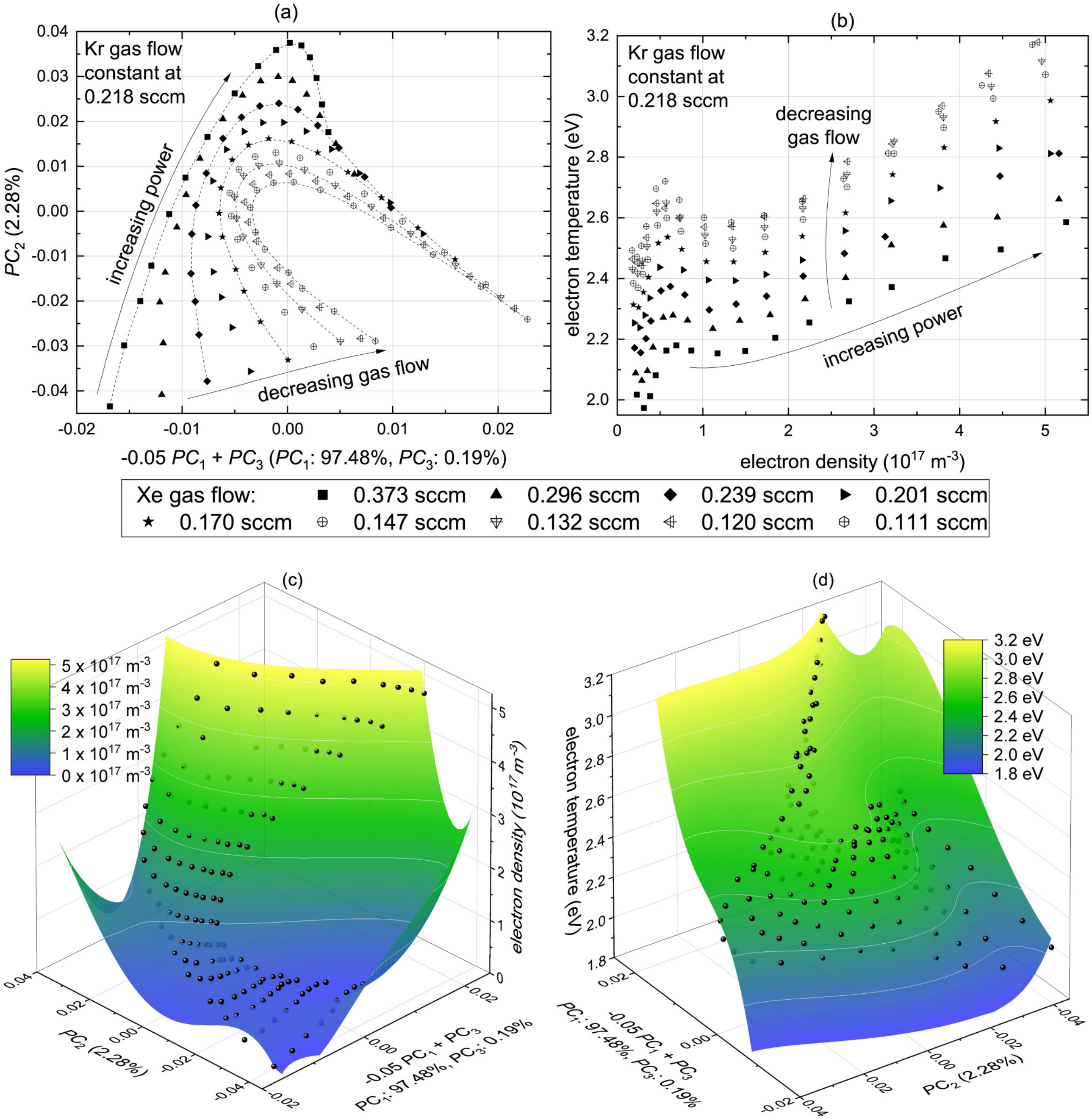

FIG. 6. PCA scores of the xenon/krypton mixed gas OES measurements for a constant krypton gas flow of 0.218 sccm and variable xenon gas flow (a). Like in Fig. 4(a), the three-dimensional scores are displayed in two dimensions with the *x* axis being a vector on the PC_1–PC_3 plane to better visualize the spread in the OES data. The corresponding plasma parameters from the Langmuir double probe measurements are shown in (b). The fits of the electron density (c) and temperature (d) over the modified PCA scores are the correlation between OES and plasma parameters for the mixed gas plasma with a constant krypton gas flow of 0.218 sccm.

fitting are avoided. Similar results have been obtained for the other xenon/krypton gas mixture series based on constant krypton gas flows of 0.354, 0.147, and 0.108 sccm, which are provided in the data availability statement. The results strongly suggest that a similar analysis and the establishment of a surjective mapping of the PC scores of spectra onto the corresponding plasma parameters are also possible for datasets taken of xenon/krypton gas mixtures with constant fractions of xenon and krypton.

The situation is different when simultaneously performing a PCA of the full dataset, i.e., of all spectra taken at different xenon and krypton gas flows and rf powers. In this case, we cannot find a 2D plane in the coordinate space of the spectra where the data points representing the spectra are clearly separated. This means that at least a third principal component based coordinate axis is required to achieve a full separation of the data points representing the spectra. However, this is somewhat anticipated as three external control parameters, xenon gas flow, krypton gas flows, and rf power, are variable in this situation. However, it should still be possible to establish a corresponding surjective mapping between PC scores and plasma parameters, but it will be of higher dimensionality than two-dimensional.

IV. CONCLUSION

We have developed an empirical approach for correlating optical emission spectra of gas plasmas obtained at different operational points with the corresponding plasma parameters. For this purpose, we measured the optical emission spectra of xenon, krypton, and xenon/krypton mixed plasmas at different operational points and simultaneously performed Langmuir probe measurements. The different operational points were defined by tuning two external parameters, the propellant gas flow (in the case of the gas mixtures, the gas flow of one constituent, while keeping that of the other constant), as well as the power coupled into the plasma for each set of combined optical emission and Langmuir measurements. The Langmuir measurements at each operation point were analyzed to extract electron temperature and electron density. For each set of optical emission spectra, a principal component analysis was conducted in order to present the differences in the set of spectra by a reduced number of characteristic coordinates based on the principal components. For all sets of spectra, it was possible to unambiguously characterize each spectrum of the set by two such characteristic coordinates only. This was demonstrated for xenon by using a projection method and for krypton by using a u–v mapping method. In a corresponding, two-dimensional plot in the plane spanned by these two coordinates, the data points representing the spectra can be well separated. This separation allows us to parameterize the plasma parameters as a function of the two coordinates, i.e., to establish a surjective mapping of the optical spectra onto the plasma parameters. In particular, the finding that this approach is successful for rather complex plasmas, such as those of gas mixtures, fortifies our view that the approach will also be applicable to various types of alternative propellants in future studies, for example, iodine, whose plasma is difficult to describe by microscopic theories. Having established such a reference set by simultaneously performing optical emission spectroscopy and Langmuir measurements, the next step is to employ the surjective mappings for a non-invasive determination of the plasma properties of unknown plasmas provided the same gas is used and the operational parameters lie within those of the reference set. Such plasmas may be those inside an ion source or ion thruster where an invasive probe, such as a Langmuir probe, may not be used as it may affect the plasma properties (e.g., in the case of very small discharge vessels) or where no suitable access for the probe is available (e.g., in electric thrusters that shall be qualified for space). Future studies may also examine the spatial distributions of the plasma parameters inside a RIT using this approach. The presented method of non-invasively determining the plasma parameters by optical spectroscopy will considerably contribute to a better understanding of ion thrusters and to speeding up their development and qualification for space.

ACKNOWLEDGMENTS

Benny Nauschütt is grateful for receiving a Ph.D. studentship in the framework of the JLU-Ariane Group Graduate School "Radio frequency ion thrusters." This work was supported by ERDF within the Horizon 2020 program (Innovation Lab "Rough ambient physics").

AUTHOR DECLARATIONS

Conflict of Interest

The authors have no conflicts to disclose.

DATA AVAILABILITY

The datasets used and/or analyzed during the current study are available from JLUdata under the link "http://dx.doi.org/10.22029/jlupub-234" for the xenon and mixed gas measurements and "http://dx.doi.org/10.22029/jlupub-300" for the krypton measurements.

REFERENCES

[1] S. Mazouffre, "Electric propulsion for satellites and spacecraft: Established technologies and novel approaches," Plasma Sources Sci. Technol. **25**, 033002 (2016).

[2] K. Holste, P. Dietz, S. Scharmann, K. Keil, T. Henning, D. Zschätzsch, M. Reitemeyer, B. Nauschütt, F. Kiefer, F. Kunze, J. Zorn, C. Heiliger, N. Joshi, U. Probst, R. Thüringer, C. Volkmar, D. Packan, S. Peterschmitt, K. T. Brinkmann, H.-G. Zaunick, M. H. Thoma, M. Kretschmer, H. J. Leiter, S. Schippers, K. Hannemann, and P. J. Klar, "Ion thrusters for electric propulsion: Scientific issues developing a niche technology into a game changer," Rev. Sci. Instrum. **91**, 061101 (2020).

[3] G. Karabadzhak, Y.-H. Chiu, S. Williams, and R. Dressler, *Hall Thruster Optical Emission Analysis Based on Single Collision* (American Institute of Aeronautics and Astronautics, 2001).

[4] J. Sommerville and L. King, "An optical diagnostic for xenon Hall thrusters including metastable contributions," in *42nd AIAA/ASME/SAE/ASEE Joint Propulsion Conference and Exhibit* (American Institute of Aeronautics and Astronautics, 2006).

[5] R. Welle, *Availability Considerations in the Selection of Inert Propellants for Ion Engines* (American Institute of Aeronautics and Astronautics, 1990).

[6] R. Welle, *Xenon and Krypton Availability for Electric Propulsion—An Updated Assessment* (American Institute of Aeronautics and Astronautics, 1993).

[7] K. H. Groh, H. W. Loeb, and H. W. Velten, "Performance data comparison of the inert gas RIT 10," J. Spacecrafts Rockets **21**, 360–365 (1984).

[8] H. Bassner and K. Groh, "A 50 mn RIT thruster assembly for application to heavy geostationary satellites," in *31st Joint Propulsion Conference and Exhibit* (AIAA, 1995), p. 3068.

[9] V. Kim, G. A. Popov, V. Kozlov, A. Skrylnikov, and D. Grdlichko, "Investigation of SPT performance and particularities of its operation with Kr and Kr/Xe mixtures" in *International Electric Propulsion Conference, IEPC-01-065, Pasadena, CA* (ERPS, 2001).

[10]A. Bugrova, A. Morozov, A. Lipatov, A. Bishaev, V. Kharchevnikov, and M. Kozintseva, "Integral and spectral characteristics of ATON stationary plasma thruster operating on krypton and xenon," IEPC Paper **366**, 2003 (2003).

[11]J. A. Linnell and A. D. Gallimore, "Internal plasma potential measurements of a Hall thruster using xenon and krypton propellant," Phys. Plasmas **13**, 093502 (2006).

[12]J. A. Linnell and A. D. Gallimore, "Efficiency analysis of a Hall thruster operating with krypton and xenon," J. Prop. Power **22**, 1402–1418 (2006).

[13]H. Löb, "Ein elektrostatisches Raketentriebwerk mit Hochfrequenzionenquelle," Astronaut. Acta **8**, 49 (1962).

[14]H. Löb and J. Freisinger, *Ionenraketen* (Vieweg+Teubner Verlag, 1967).

[15]D. M. Goebel and I. Katz, *Fundamentals of Electric Propulsion*, 1st ed. (John Wiley & Sons, 2008).

[16]J. Beattie, R. Robson, and J. Williams, *Flight Qualification of an 18-mN Xenon Ion Thruster* (AIAA, 1993).

[17]V. Rawlin, J. Sovey, J. Anderson, and J. Polk, *NSTAR Flight Thruster Qualification Testing* (American Institute of Aeronautics and Astronautics, 1998).

[18]D. A. Herman, "Nasa's evolutionary xenon thruster (next) project qualification propellant throughput milestone: Performance, erosion, and thruster service life prediction after 450 kg," in *JANNAF 7th Modeling and Simulation, 5th Liquid Propulsion, and 4th Spacecraft Propulsion Joint Subcommittee Meeting* (NASA Technical Reports Server 2010), pp. 3–7.

[19]V. I. Demidov, S. V. Ratynskaia, and K. Rypdal, "Electric probes for plasmas: The link between theory and instrument," Rev. Sci. Instrum. **73**, 3409–3439 (2002).

[20]J. Benedikt, H. Kersten, and A. Piel, "Foundations of measurement of electrons, ions and species fluxes toward surfaces in low-temperature plasmas," Plasma Sources Sci. Technol. **30**, 033001 (2021).

[21]Y. Chiu, B. L. Austin, S. Williams, R. A. Dressler, and G. F. Karabadzhak, "Passive optical diagnostic of Xe-propelled Hall thrusters. I. Emission cross sections," J. Appl. Phys. **99**, 113304 (2006).

[22]G. F. Karabadzhak, Y. Chiu, and R. A. Dressler, "Passive optical diagnostic of Xe propelled Hall thrusters. II. Collisional-radiative model," J. Appl. Phys. **99**, 113305 (2006).

[23]T. S. Matlock, C. W. Larson, W. A. Hargus Jr, and M. R. Nakles, "An inversion method for reconstructing Hall thruster plume parameters from the line integrated measurements (postprint)," Technical Report, 2007.

[24]J. Yang, S. Yokota, R. Kaneko, and K. Komurasaki, "Diagnosing on plasma plume from xenon Hall thruster with collisional-radiative model," Phys. Plasmas **17**, 103504 (2010).

[25]L.-Q. Wei, W.-B. Li, Y.-J. Ding, X.-M. Zhu, Y.-F. Wang, J.-F. Hu, S.-L. Yan, and D.-R. Yu, "A photographic method for in-orbit measurement of electron temperature distribution in the plume of Hall thrusters," Plasma Sources Sci. Technol. **27**, 084002 (2018).

[26]Y. Wang, Y.-F. Wang, X.-M. Zhu, O. Zatsarinny, and K. Bartschat, "A xenon collisional-radiative model applicable to electric propulsion devices: I. Calculations of electron-impact cross sections for xenon ions by the Dirac B-spline R-matrix method," Plasma Sources Sci. Technol. **28**, 105004 (2019).

[27]X.-M. Zhu, Y.-F. Wang, Y. Wang, D.-R. Yu, O. Zatsarinny, K. Bartschat, T. V. Tsankov, and U. Czarnetzki, "A xenon collisional-radiative model applicable to electric propulsion devices: II. Kinetics of the 6s, 6p, and 5d states of atoms and ions in Hall thrusters," Plasma Sources Sci. Technol. **28**, 105005 (2019).

[28]M. R. Nakles and T. S. Matlock, "Hall thruster near-field plume characterization through optical emission spectroscopy" in *International Electric Propulsion Conference, IEPC-2019-246, Vienna, Austria* (ERPS, 2019).

[29]B. T. Nauschütt, L. Chen, K. Holste, and P. J. Klar, "Non-invasive assessment of plasma parameters inside an ion thruster combining optical emission spectroscopy and principal component analysis," EPJ Tech. Instrum. **8**, 13 (2021).

[30]H. Abdi and L. J. Williams, "Principal component analysis," Wiley Interdiscip. Rev. Comput. Stat. **2**, 433–459 (2010).

[31]J. Vlcek, "A collisional-radiative model applicable to argon discharges over a wide range of conditions. I. Formulation and basic data," J. Phys. D: Appl. Phys. **22**, 623–631 (1989).

[32]J. Vlcek and V. Pelikan, "A collisional-radiative model applicable to argon discharges over a wide range of conditions. II. Application to low-pressure, hollow-cathode arc and low-pressure glow discharges," J. Phys. D: Appl. Phys. **22**, 632–643 (1989).

[33]A. Bogaerts, R. Gijbels, and J. Vlcek, "Collisional-radiative model for an argon glow discharge," J. Appl. Phys. **84**, 121–136 (1998).

[34]A. Bogaerts, R. Gijbels, and J. Vlcek, "Modeling of glow discharge optical emission spectrometry: Calculation of the argon atomic optical emission spectrum," Spectrochim. Acta Part B **53**, 1517–1526 (1998).

[35]S. Iordanova and I. Koleva, "Optical emission spectroscopy diagnostics of inductively-driven plasmas in argon gas at low pressures," Spectrochim. Acta Part B **62**, 344–356 (2007).

[36]N. Tian-Ye, C. Jin-Xiang, L. Lei, L. Jin-Ying, W. Yan, W. Liang, and L. You, "A comparison among optical emission spectroscopic methods of determining electron temperature in low pressure argon plasmas," Chin. Phys. **16**, 2757–2763 (2007).

[37]G. P. Canal, H. Luna, R. M. O. Galvão, and R. Castell, "An approach to a non-LTE Saha equation based on the Druyvesteyn energy distribution function: A comparison between the electron temperature obtained from OES and the Langmuir probe analysis," J. Phys. D: Appl. Phys. **42**, 135202 (2009).

[38]J. B. Boffard, C. C. Lin, and C. A. DeJosephJr, "Application of excitation cross sections to optical plasma diagnostics," J. Phys. D: Appl. Phys. **37**, R143–R161 (2004).

[39]J. B. Boffard, R. O. Jung, C. C. Lin, L. E. Aneskavich, and A. E. Wendt, "Argon 420.1–419.8 nm emission line ratio for measuring plasma effective electron temperatures," J. Phys. D: Appl. Phys. **45**, 045201 (2012).

[40]J. B. Boffard, R. O. Jung, C. C. Lin, and A. E. Wendt, "Optical emission measurements of electron energy distributions in low-pressure argon inductively coupled plasmas," Plasma Sources Sci. Technol. **19**, 065001 (2010).

[41]X.-M. Zhu, W.-C. Chen, J. Li, and Y.-K. Pu, "Determining the electron temperature and the electron density by a simple collisional-radiative model of argon and xenon in low-pressure discharges," J. Phys. D: Appl. Phys. **42**, 025203 (2008).

[42]X.-M. Zhu and Y.-K. Pu, "Optical emission spectroscopy in low-temperature plasmas containing argon and nitrogen: Determination of the electron temperature and density by the line-ratio method," J. Phys. D: Appl. Phys. **43**, 403001 (2010).

[43]X.-M. Zhu, Y.-K. Pu, Y. Celik, S. Siepa, E. Schüngel, D. Luggenhölscher, and U. Czarnetzki, "Possibilities of determining non-Maxwellian EEDFs from the OES line-ratios in low-pressure capacitive and inductive plasmas containing argon and krypton," Plasma Sources Sci. Technol. **21**, 024003 (2012).

[44]S. Siepa, S. Danko, T. V. Tsankov, T. Mussenbrock, and U. Czarnetzki, "On the OES line-ratio technique in argon and argon-containing plasmas," J. Phys. D: Appl. Phys. **47**, 445201 (2014).

[45]R. A. Dressler, Y. Chiu, O. Zatsarinny, K. Bartschat, R. Srivastava, and L. Sharma, "Near-infrared collisional radiative model for Xe plasma electrostatic thrusters: The role of metastable atoms," J. Phys. D: Appl. Phys. **42**, 185203 (2009).

[46]X.-M. Zhu, W.-C. Chen, and Y.-K. Pu, "Gas temperature, electron density and electron temperature measurement in a microwave excited microplasma," J. Phys. D: Appl. Phys. **41**, 105212 (2008).

[47]Priti, R. K. Gangwar, and R. Srivastava, "Collisional-radiative model of xenon plasma with calculated electron-impact fine-structure excitation cross-sections," Plasma Sources Sci. Technol. **28**, 025003 (2019).

[48]V. M. Donnelly, "Plasma electron temperatures and electron energy distributions measured by trace rare gases optical emission spectroscopy," J. Phys. D: Appl. Phys. **37**, R217–R236 (2004).

[49]Y. Iida, S. Kado, and S. Tanaka, "On the application of He I collisional-radiative model to the He–H2 mixture plasmas in MAP-II divertor simulator," J. Nucl. Mater. **438**, S1237–S1240 (2013).

[50]Priti, R. K. Gangwar, and R. Srivastava, "Collisional radiative model for Ar-O_2 mixture plasma with fully relativistic fine structure cross sections," Phys. Plasmas **25**, 043517 (2018).

[51] N. Shukla, R. K. Gangwar, and R. Srivastava, "Diagnostic of Ar-CO_2 mixture plasma using a fine-structure resolved collisional radiative model," Spectrochim. Acta Part B **175**, 106019 (2021).

[52] F. Debal, J. Bretagne, M. Jumet, M. Wautelet, J. P. Dauchot, and M. Hecq, "Analysis of DC magnetron discharges in Ar-N_2 gas mixtures. comparison of a collisional-radiative model with optical emission spectroscopy," Plasma Sources Sci. Technol. **7**, 219–229 (1998).

[53] E. B. Saloman, "Energy levels and observed spectral lines of xenon, Xe I through Xe LIV," J. Phys. Chem. Ref. Data **33**, 765–921 (2004).

[54] O. Cheshnovsky, B. Raz, and J. Jortner, "Electronic energy transfer in rare gas mixtures," J. Chem. Phys. **59**, 3301–3307 (1973).

[55] J. D. Cook and P. Leichner, "Collisional and radiative excitation transfers in Kr-Xe mixtures: Quenching of Kr," Phys. Rev. A **31**, 90 (1985).

[56] J. D. Cook and P. Leichner, "Collisional and radiative excitation transfers in Kr-Xe mixtures: Emissions from the Xe (3 p 1) resonant level and the Xe first continuum region," Phys. Rev. A **43**, 1614 (1991).

[57] B. Krylov, G. Gerasimov, A. Morozov, A. Arnesen, R. Hallin, and F. Heijkenskjold, "Energy transfer studies in krypton-xenon mixtures excited in a cooled dc discharge," Eur. Phys. J. D **8**, 227–239 (2000).

[58] G. Zvereva and A. Loginov, "Excitation transfer in the plasma of a barrier discharge in a krypton-xenon mixture," Opt. Spectrosc. **90**, 502–507 (2001).

[59] E. J. McGuire, "Electron ionization cross sections in the born approximation," Phys. Rev. A **16**, 62 (1977).

[60] D. Margreiter, H. Deutsch, and T. Märk, "A semiclassical approach to the calculation of electron impact ionization cross-sections of atoms: From hydrogen to uranium," Int. J. Mass Spectrom. Ion Processes **139**, 127–139 (1994).

[61] D.-W. Chang and P. L. Altick, "Doubly, singly differential and total ionization cross sections of rare-gas atoms," J. Phys. B At. Mol. Opt. Phys. **29**, 2325 (1996).

[62] A. A. Sorokin, L. A. Shmaenok, S. V. Bobashev, B. Möbus, M. Richter, and G. Ulm, "Measurements of electron-impact ionization cross sections of argon, krypton, and xenon by comparison with photoionization," Phys. Rev. A **61**, 022723 (2000).

[63] R. O. Jung, J. B. Boffard, L. W. Anderson, and C. C. Lin, "Electron-impact excitation cross sections from the xenon $J = 2$ metastable level," Phys. Rev. A **72**, 022723 (2005).

[64] M. A. Stevenson, L. R. Hargreaves, B. Lohmann, I. Bray, D. V. Fursa, K. Bartschat, and A. Kheifets, "Fully differential cross-section measurements for electron-impact ionization of neon and xenon," Phys. Rev. A **79**, 012709 (2009).

[65] K. Holste, W. Gärtner, D. Zschätzsch, S. Scharmann, P. Köhler, P. Dietz, and P. J. Klar, "Performance of an iodine-fueled radio-frequency ion-thruster," Eur. Phys. J. D **72**, 9 (2018).

[66] P. Dietz, W. Gärtner, Q. Koch, P. E. Köhler, Y. Teng, P. R. Schreiner, K. Holste, and P. J. Klar, "Molecular propellants for ion thrusters," Plasma Sources Sci. Technol. **28**, 084001 (2019).

[67] H. Henke, *Elektromagnetische Felder : Theorie und Anwendung* (Springer Berlin Heidelberg, Berlin, 2015).

[68] E. O. Johnson and L. Malter, "A floating double probe method for measurements in gas discharges," Phys. Rev. **80**, 58–68 (1950).

[69] S. Bhattarai, "Interpretation of double langmuir probe I-V characteristics at different ionospheric plasma temperatures," Am. J. Eng. Appl. Sci. **10**, 882–889 (2017).

[70] A. Kramida and Y. Ralchenko, "NIST atomic spectra database, NIST standard reference database 78" (1999).

[71] J. Simon, U. Probst, and P. J. Klar, "Development of a radio-frequency generator for rf ion thrusters," in *34th International Electric Propulsion Conference, Hyogo-Kobe, Japan* (Aerospace Technology Japan, 2015).

[72] J. E. Junker, U. Probst, and P. J. Klar, "Development of a full bridge series resonant radio-frequency generator for optimized rit operation," in *36th International Electric Propulsion Conference, Vienna, Austria* (ERPS, 2019).

[73] E. B. Saloman, "Energy levels and observed spectral lines of krypton, Kr I through Kr XXXVI," J. Phys. Chem. Ref. Data **36**, 215–386 (2007).

[74] A. J. Izenman, "Linear discriminant analysis," in *Modern Multivariate Statistical Techniques*, Springer Texts in Statistics (Springer, New York, 2013), pp. 237–280.

[75] V. P. Pauca, J. Piper, and R. J. Plemmons, "Nonnegative matrix factorization for spectral data analysis," Linear Algebra Appl. **416**, 29–47 (2006).

[76] R. L. Gorsuch, *Factor Analysis* (Psychology Press, 2013).

[77] J. B. Boffard, R. O. Jung, C. C. Lin, L. E. Aneskavich, and A. E. Wendt, "Optical diagnostics for characterization of electron energy distributions: Argon inductively coupled plasmas," Plasma Sources Sci. Technol. **20**, 055006 (2011).

[78] A. Reeh, U. Probst, and P. J. Klar, "Global model of a radio-frequency ion thruster based on a holistic treatment of electron and ion density profiles," Eur. Phys. J. D **73**, 232 (2019).

[79] P. Dietz, A. Reeh, K. Keil, K. Holste, U. Probst, P. J. Klar, and C. Volkmar, "Global models for radio-frequency ion thrusters," EPJ Tech. Instrum. **8**, 10 (2021).